Three-point bending behavior of a Au nanowire studied by in-situ Laue micro-diffraction

Z. Ren, T. Cornelius, C. Leclere, A. Davydok, J.-S. Micha, O. Robach, G. Richter, O. Thomas

Three-point bending behavior of a Au nanowire studied by *in-situ* Laue micro-diffraction

Z. Ren[1], T.W. Cornelius[1*], C. Leclere[1], A. Davydok[1], J.-S. Micha[2, 3], O. Robach[2, 3], G. Richter[4], O. Thomas[1]

[1]*Aix Marseille Univ, Univ de Toulon, CNRS, IM2NP, Marseille, France*

[2]*CRG-IF BM32 Beamline at the European Synchrotron (ESRF), CS40220, 38043 Grenoble Cedex 9, France*

[3]*Université Grenoble Alpes, CEA/INAC, 17 rue des Martyrs, 38054 Grenoble, France*

[4]*Max Planck Institute for Intelligent Systems, Heisenbergstrasse 3, 70569 Stuttgart, Germany*

**Corresponding author*

Thomas W. Cornelius

IM2NP UMR 7334 CNRS

Aix-Marseille Université

Faculté des Sciences, Campus de St Jérôme - Case 262

Avenue Escadrille Normandie Niemen

13397 Marseille Cedex 20

France

Abstract (max 200-250 words)

The elastic and plastic deformation of a gold nanowire tested in three-point bending configuration using the custom-built scanning force microscope SFINX was studied *in-situ* by Laue micro-diffraction. A new data treatment method, which bases on the integration of diffraction patterns recorded along the deformed nanostructure, is introduced visualizing both movement and shape of the diffraction peaks as a function of the measurement position. Besides bending, torsion is evidenced during the elastic deformation originating from a misalignment of the SFINX-tip of the order of 60 nm with respect to the nanowire center. As demonstrated by *post-mortem* Laue micro-diffraction maps, the plastic deformation is governed by the storage of geometrically necessary dislocations. Analyzing the shape of the diffraction peaks, the activation of two unexpected slip systems is found which does not coincide with the slip systems with the highest resolved shear stress. These unexpected slip systems are probably related to the dislocation nucleation process at the clamping point, which is influenced by the local curvature.

Keywords: plasticity, geometrically necessary dislocations (GNDs), nanowire, *in-situ* three-point bending test, Laue micro-diffraction

This manuscript was accepted by J. Appl. Phys. Click here to see the version of record.

1. Introduction

Since the first mechanical tests on microwhiskers in the 1950s [1,2], studies have demonstrated that the mechanical behavior of micro- and nanostructures differ from their bulk counterpart e.g. showing higher yield strengths with values near the theoretical limit of the materials for some of the defect-free macro-pillars and nanowires [3,4]. Most of these micro- and nano-mechanical tests were conducted in uniaxial testing configuration applying either a tensile or a compressive stress. When plasticity sets in, dislocations tend to glide through the structures before they can interact with each other [5], at variance with what happens at macroscopic scales. In tension tested single-crystalline Au nanowires, for example, dissociated dislocations are generated as leading partials with higher Schmid factors. After nucleation, these partial dislocations rapidly glide through the nanowire leaving stacking faults behind, which accumulate and eventually lead to Σ3 twin formation [6–8].

Bending is evidently a more complex mechanical test, which is less well studied especially at the nanoscale. However, the understanding of bending behavior is crucial for many practical situations such as for flexible electronics or MEMS devices. As pointed out by Nye in the 1950s [9], in bending tests, dislocations can be non-uniformly stored to minimize the strain energy during mechanical loading, and are thus required for the compatible deformation of various parts of the crystal. Recently, Konijnenberg *et al*. demonstrated that the bending deformation for FIB fabricated cantilever micro-beams is mainly accommodated by the storage of geometrically necessary dislocations (GNDs) [10]. Contrary to these micron-scale cases, some recent molecular dynamics (MD) simulations suggest that at the nanoscale the bending is accommodated by the formation of wedge-shaped twins similar to the ones observed in

uniaxial tension tests [11,12]. While most studies reported in literature focused on the cantilever bending of micrometer sized beams prepared via FIB milling [10,13–18], reports on plastic bending experiments for defect-scarce nanostructures are limited. To further explore the deformation mechanism for the bending at the nanoscale, *in-situ* three-point bending test is performed on an as-grown Au nanowire in combination with Laue micro-diffraction in the present work. Based on the rotation of the Au crystal along the nanowire, the deformation profile is extracted, which is further compared with finite element method (FEM) simulations. Combined with *post-mortem* Laue micro-diffraction maps and SEM characterization, the activated slip systems are discussed shedding additional light on mechanisms of plastic bending in defect-scarce nanomaterials.

2. Experimental

In-situ three-point bending tests are performed using the custom designed scanning force microscope SFINX [19], which is installed at the French CRG-IF beamline BM32 at the European Synchrotron (ESRF) in Grenoble (France) as schematically illustrated in the Fig. 1(a). The incident polychromatic X-ray beam with an effective energy range between 5 and 25 keV is focused down to 400 nm (V) x 500 nm (H) on the sample surface using a pair of Kirkpatrick-Baez (KB) mirrors. The fluorescence yield is monitored using a Röntec XFlash 1001 energy-resolved point detector and the diffracted X-rays are recorded by a MarCCD165 detector with 2048 x 2048 pixels of 80 µm in size, which is mounted at a distance of 70 mm and 90° with respect to the incident beam (angular resolution of the detector around 0.065˚).

Single-crystalline and nominally defect-free Au nanowires were grown by physical vapor deposition on carbon coated tungsten or molybdenum substrates [3]. For three-point bending

tests, the growth substrate was rubbed against a Si substrate patterned with 10 µm wide and 1.5 µm deep Si micro-trenches, transferring the as-grown Au nanowire. Some of the randomly distributed Au nanowires cross Si micro-trenches forming self-suspended nano-bridges. To avoid any sliding during mechanical testing, these Au nanowires are clamped to the Si supports by depositing carbon from the residual gas in a SEM chamber. As illustrated in Fig. 1(b), the growth direction of these Au nanowires is along $[01\bar{1}]$ [7] and the Au nanowires lie down on the Si substrate with one of their <111> side facets [20]. The length of the nanowire is around 19 µm and the width of the nanowire is about 360nm, which is similar to the size of the X-ray beam. Bragg coherent X-ray diffraction imaging as well as Laue micro-diffraction on similar nanowires revealed that the suspended nanowire parts are free of both strain and defects However, blurred diffraction patterns recorded for nanowire parts on top of the Si supports suggest that the transfer process might affect the strain state in these nanowire sections [20].

For nano-mechanical testing, firstly, pre-selected nanowires are located by AFM imaging using SFINX (noise around 10 nm) and mapping of the Au L_{III} fluorescence with the X-ray beam. Subsequently, the SFINX-tip is positioned above the center of the self-suspended nanowire and then lowered at a constant speed of 2 nm/s using the piezoelectric z-stage installed in SFINX. The loading process is interrupted after each 50 nm displacement of the piezoelectric stage and Laue micro-diffraction patterns are recorded along the deflected nanowire in steps of 770 nm by rotating the downstream KB mirror in steps of 0.004° (calibration factor = 192 µm/degree). Each KB scan takes around 3 min, where 13 diffraction patterns are recorded along the suspended part of the nanowire. In this way, the complete deformation profile of the deflected nanowire is measured via the recently developed KB scan approach, which avoids potentially

This manuscript was accepted by J. Appl. Phys. Click here to see the version of record.

destructive vibrations to the nano-mechanical testing equipment [21].

After the complete retraction of the SFINX-tip, a Laue micro-diffraction map is recorded along the deformed Au nanowire in steps of 500 nm employing the sample translation stage. The finer step size yields a diffraction map with higher intensity and spatial resolution. However, the measurement positions are also slightly difference between the *in situ* and *post mortem* diffraction map, which is compensated by comparing both of them to the SEM image. A background Laue micro-diffraction pattern is recorded on the bare Si surface a few micrometers distant to the Au nanowire. The nanowire deformation is additionally simulated within continuum elasticity by the finite element method (FEM) using COMSOL Multiphysics taking into account the exact nanowire geometry, the elastic constants of bulk Au, and considering the Au nanowire being thoroughly clamped.

3. Laue microdiffraction data analysis

For data treatment, the background diffraction pattern is first subtracted from the nanowire diffraction patterns, removing the Si diffraction peaks and enhancing the visibility of the Au Laue spots (see Fig. S1 in supplementary material). The Au diffraction patterns are then indexed employing the LaueTools software [22], and the Au crystalline orientation is extracted as an orientation matrix (called UB matrix in the following) considering at least eight Laue spots (The X direction of the lab coordinates is along the beam direction, the Z direction perpendicular to the 2D detector). Employing this indexing process, one-dimensional orientation maps along the nanowire are generated, which are presented as the deviation angles θ for three distinct Au crystalline directions (Au [111], Au $[01\bar{1}]$, Au $[\bar{2}11]$) (further details can be found in the supplementary material). These three crystalline directions correspond to the top surface

direction, the nanowire growth axis, and the direction perpendicular to the loading plane, respectively.

One-dimensional orientation plots present the rotations of the crystal lattice which are caused either by elastic deformation or by the presence of unpaired dislocations. However, for weak diffracting objects such as the nanowires, extracting the absolute orientation by indexation is sometimes hindered by some eventual blurring of the diffraction peaks. Furthermore, as pointed out by Nye [9], three-dimensional measurements of the crystal orientation are needed to calculate the curvature of the atomic lattice and to deduce the density of stored GNDs. Extracting the GND configuration from one-dimensional orientation maps requires additional assumptions, which compensate for components missing in Nye's tensor [23]. Thus, in the present work, an alternative experimental strategy is developed to further track the lattice rotation along the nanowire under mechanical testing. In this approach, the background subtracted diffraction patterns recorded at the same deformation state are summed up generating integrated diffraction patterns. Thus, each integrated diffraction pattern reflects a complete orientation profile of the deflected Au nanowire. Analogous to diffraction patterns measured using a pencil beam oriented parallel to the nanowire long axis, the displacements and the shape of the Au Laue spots along the nanowire are clearly visualized as continuous paths on the detector (see Mov. S1 in the supplementary material). Compared to a pencil beam measurement, the experimental approach described in the present work, however, provides additional information about both the measurement position and the shape of individual Laue spots. Similar to ref. [24], quantitative analysis of each individual diffraction pattern is then achieved by comparing these paths to the ones produced by the relative rotation

This manuscript was accepted by J. Appl. Phys. Click here to see the version of record.

of the Au crystal along the nanowire around defined crystallographic axes.The orientation matrix after a certain rotation is described with the following equation

$$\mathrm{UB}_{expected} = \mathrm{UB}_{origin} \cdot \mathrm{C} \cdot \begin{bmatrix} \cos(\omega) & -\sin(\omega) & 0 \\ \sin(\omega) & \cos(\omega) & 0 \\ 0 & 0 & 1 \end{bmatrix} \cdot C^{-1} \quad (1)$$

where ω is the rotation angle and C is the transformation matrix between the crystal coordinates (x, y, z axis along the three principal crystalline directions) and rotation coordinates (z' axis is the rotation axis, x', y' axes are orthogonal to the z'). Considering the geometrical parameters of the detector, these different orientation matrices can be expressed as different positions of the diffraction intensity on the detector, which eventually predicts the movement and elongation direction of the diffraction peaks after a certain rotation.

The movement of the diffraction peaks gives access to the rotation along the nanowire similar to 1D orientation maps. For a bending in the vertical plane, the Au crystal along the nanowire rotates around the $[\bar{2}11]$ axis in the present work. The calculated deviation angles for the top surface direction (Au $[111]$) and the growth direction (Au $[01\bar{1}]$) of the nanowire coincide with the bending angles of the nanowire, while the deviation angle for the direction perpendicular to the loading plane (Au $[\bar{2}11]$) is zero. The transformation matrix C can be written as

$$C = \begin{bmatrix} 0 & 1/\sqrt{3} & -2/\sqrt{6} \\ 1/\sqrt{2} & 1/\sqrt{3} & 1/\sqrt{6} \\ -1/\sqrt{2} & 1/\sqrt{3} & 1/\sqrt{6} \end{bmatrix} \quad (2)$$

Combined with equation 1, the expected orientation matrix after this rotation is calculated, which predicts the expected path of the diffraction peaks for a pure vertical bending.

Considering edge dislocations, the 12 slip systems in FCC crystals induce rotations around the 12 different <112> axes, thus generating 12 independent movements and streaking directions of the Laue spots (as illustrated by Fig. S3 in the supplementary material). In Laue diffraction formalism [25,26], the principal elongation direction of the Laue spots is usually referred as ξ direction, which is perpendicular to both the dislocation line direction $\vec{\tau}$ and the momentum transfer vector $\overrightarrow{G_{hkl}}$. While the activation of a single slip system causes movement and streaking of the diffraction peaks in a well-defined crystallographic direction, the simultaneous activation of multiple slip systems results in a movement that is defined by a linear combination of the corresponding crystalline rotations. Hofmann *et al*. [27] illustrated experimentally that already a single dislocation in a nanostructure leads to large bending angles as compared with what happens in the bulk. The induced pronounced rotation field may significantly afffect the peak shape as it will be demonstrated for a plastically deformed Au nanowire in the present work. This combination of diffraction peak shape analysis with a simple model provides additional information about the local rotation field within the probed volume giving access both to the activated slip systems and to the spatial distribution of the stored dislocations (see section 4.2).

4. Results

A sequence of integrated background subtracted Laue micro-diffraction patterns at different deformation states during a three-point bending test is presented in Fig. 2 with the inset displaying the enlarged area around the Au 222 Laue spot. A movie showing the complete evolution of the integrated diffraction patterns can be found in the supplementary material (see Mov. S2). In the initial state (see Fig. 2(a)), when the SFINX-tip does not touch the nanowire, a

This manuscript was accepted by J. Appl. Phys. Click here to see the version of record.

slight spread of the diffraction peak positions is apparent, which corresponds to a small variation of the Au crystalline orientation on the order of 2°. This small deformation might be related to an unintentional folding of the cantilever part of the nanowire during the alignment process (see *post-mortem* SEM image in Fig. 4(a)). At a movement of the piezoelectric z-stage of 200 to 300 nm the SFINX-tip gets into contact with the nanowire and the integrated diffraction patterns start evolving continuously. With increasing load, the Laue diffraction peaks describe larger and larger elliptical paths on the detector (see Fig. 2 (b-d)). At the piezo movement of 1200 nm, the paths of the diffraction peaks split into two semi-circles, which are separated around the loading point. In a first approximation, the continuous change observed at small movements of the piezoelectric stage is attributed to the elastic bending of the Au nanowire, while the discontinuous change at Δz = 1200 nm is ascribed to plasticity.

4.1 Elastic deformation: bending + torsion

For understanding the continuous evolution of the integrated diffraction patterns, the movement of the Au 222 Laue spot on the detector recorded at the piezo movement of 1100 nm is exemplarily presented in Fig. 3(a). The displacement of the Laue spot on the detector is determined by the variation of the deviatoric strain and/or the misorientation of the Au crystal along the suspended nanowire. During bending, the deviatoric strain varies linearly through the thickness of the nanowire with an average value close to zero [28,29]. It is thus neglected within a first approximation and the displacement of the Laue spot is solely attributed to the variation of the Au crystalline orientation.

A pure bending induces a rotation around the $[\bar{2}11]$ axis along the nanowire, which corresponds to an almost horizontal displacement of the Au 222 diffraction peak as indicated by

This manuscript was accepted by J. Appl. Phys. Click here to see the version of record.

the red line in Fig. 3(a). Thus, bending alone cannot explain the observed elliptical path. Introducing an additional torsion leads to a rotation around the Au $[01\bar{1}]$ direction corresponding to a vertical displacement of the Au 222 spot on the detector (as illustrated by the black line in Fig. 3(a)). The elliptical path observed for the Au 222 Laue spot can thus be produced by combining these two kinds of rotations. From the center of the Au 222 Laue spots at each of the 13 measurement positions along the suspended nanowire (highlighted by red full dots in Fig. 3(a)), the bending and torsion profiles are deduced as presented by red and blue open circles in Fig. 3(b), respectively. Close to the Si supports (positions 1 and 13), the Au 222 Laue spot is located next to the Si 004 diffraction peak indicating that the crystalline orientation of the Au nanowire is close to its initial state. Thus, bending and torsion angles are set to zero at these two positions. For the suspended part of the nanowire, the bending angle exhibits an expected sine like variation ranging from -6° to +6° with the maxima observed at around half-distance between the clamping and the loading point (positions 4 and 10). In contrast, the torsion angle increases linearly reaching a maximum of 9° at the loading position (position 7) where the bending angle is approximately zero (see Fig. 3(b)). According to FEM simulations, this additional torsion is caused by a misalignment ε of the SFINX-tip with respect to the center of the nanowire width. As evidenced in Fig. 3(b), the bending and torsion profiles measured in the experiment are well reproduced considering an applied force of 2.1 µN and a misalignment of the SFINX-tip of 57 nm.

While so far, we mainly focused on the Au 222 Laue diffraction peak, similar results are obtained for the other Laue spots as illustrated by Fig. 2(d). The continuous evolution of the integrated diffraction patterns thus directly translates into an increasing bending and torsion of

the nanowire during the three-point bending test. The peak-to-peak values for the bending and the torsion angles at each deformation state are inferred from height and width of the ellipse described by the Au 222 Laue spots in the integrated diffraction patterns, which are displayed in Fig. 3(c) and (d), respectively. With increasing movement of the piezoelectric stage the peak-to-peak value of the bending angle increases from 2° to 13° and the maximum torsion angle increases from 0° to 9°. While the bending increases rapidly at small loads and starts to saturate at larger Δz, the torsion shows a steeper slope for higher loads making it important for large deformations. FEM simulations describe well the experimental bending when defining Δz = 270 nm as the contact point of the SFINX-tip. The discrepancies between the simulation and the experimental bending angles at small Δz may be attributed either to the slight deformation of the Au nanowire at the initial state or to the intermittent contact at small loads. Regarding the torsion, the experimental data do not show a continuous evolution and, hence cannot be reproduced by FEM simulations considering the same misalignment ε over the whole range. Different misalignments ε (20 and 60 nm) of the SFINX-tip with respect to the center of the nanowire width do not significantly affect the simulated bending angles, whereas the simulated torsion increases almost linearly with ε. The scattered torsion thus might indicate that the SFINX-tip slides on the nanowire during the loading process leading to the misalignment in the range between 20 nm and 60 nm.

4.2 Plasticity

4.2.1 Storage of GNDs

At the piezo movement of 1300 nm, the SFINX-tip is retracted from the nanowire. A one-dimensional orientation map of the Au nanowire after complete unloading, which is

superimposed with a *post-mortem* SEM image, is presented in Fig. 4(a). According to the movement direction of the Laue spots in the corresponding integrated diffraction pattern (see Fig. 4(b)), the nanowire is divided into three sections, which are marked with four points. In the center of the self-suspended nanowire, the *post-mortem* SEM image reveals a kink evidencing the plastic deformation of the nanowire. In vicinity to the kink, Laue micro-diffraction data are missing because the diffraction intensity was below the detection limit suggesting a strongly perturbed crystalline lattice, i.e. a large number of stored dislocations. The discontinuous evolution of the integrated diffraction pattern at the piezo movement of 1200 nm (see Fig. 2(e)) might indicate the kink formation around the loading position. Close to the Si supports (position i and iv), all deviation angles are close to 0° indicating that the nanowire is thoroughly clamped during the deformation. Between the Si support and the kink (from position i to ii, and from position iv to iii), the diffraction peaks move continuously on the detector implying a continuous variation of the Au crystalline orientation. The deviation angles of the wire direction (Au $[01\bar{1}]$) and the top surface direction (Au $[111]$) increase continuously to 13° and -16.5° when approaching the nanowire center from the left-hand side and the right-hand side, respectively. On the other hand, the deviation angle along the Au $[\bar{2}11]$, which is the direction perpendicular to the loading plane, does not exceed 4° all along the nanowire. Since the diffraction map is recorded after the complete unloading, the elastic strain within the nanowire is neglected, in a first approximation, and the large variation of the crystalline orientation observed is thus attributed to the storage of geometrically necessary dislocations (GNDs).

4.2.2 Activated slip systems

In the *post-mortem* Laue micro-diffraction map (Fig. 4(b)), the movement of the Laue spots does not coincide with any of the expected directions for the 12 slip systems generated by edge dislocations in FCC crystals (see Fig. S3 in the supplementary material). Instead, the change of the crystalline orientation shown in Fig. 4(a) can well be explained by the combination of two simultaneously activated slip systems. Inverse pole figures calculated for the <112> poles (as presented in Fig. S4 in the supplementary material) reveal that the measured crystalline orientation follows very accurately the expected rotation induced by the $[01\bar{1}](111)$ slip system for the $[\bar{1}\bar{2}1]$ pole and the $[\bar{2}\bar{1}1]$ pole, whereas it does not match any of the expected rotations generated by other slip systems for the other <112> poles. This leaves only two possibilities for a second activated slip system: either $[101](\bar{1}11)$ or $(011)[1\bar{1}1]$. The shape of the diffraction peaks give access to the local rotation field induced by GNDs stored in the material, and thus provide additional information on the activated slip systems. Comparison of the streaking directions induced by the two aforementioned slip systems with the shape of the diffraction peaks (as illustrated by Fig. S5 in the supplementary material) yields a good accordance between the streaking caused by $[101](\bar{1}11)$ dislocations and the vertical spread of the Laue spots, whereas the streaking direction induced by $(011)[1\bar{1}1]$ dislocations does not show any correspondence with the shape of the Laue spots. Thus, the GNDs stored are inferred as combination of $[01\bar{1}](111)$ and $[101](\bar{1}11)$ slip systems, which induces rotations around the Au $[\bar{2}11]$ and the Au $[12\bar{1}]$ axes. The upper and lower borders of the trapezoidal shaped diffraction peaks can be well reproduced by a linear combination of rotations around these two axes with ratios of 9.5 and 5.8, respectively (see Fig. 6). While this linear combination describes

This manuscript was accepted by J. Appl. Phys. Click here to see the version of record.

well the shape of the diffraction peaks between the left Si support and the kink (positions i and ii) as well as for some of the diffraction patterns close to the right Si support (position iv), the measured Laue spots increasingly deviate from this prediction when approaching the kink from the right-hand side. This presumably is caused either by elastic strain or by additionally activated slip systems.

4.2.3 Number of stored GNDs

According to Nye [9], the plastic rotation of a crystal by an angle Δθ is directly related to the density of stored GNDs:

$$\rho_{GND} = \frac{\Delta\theta}{Lb} \tag{3}$$

where *b* is the Burger's vector, and L is the probe length along **b**. Considering a single edge dislocation and *t* being the effective thickness along the slip plane direction, the lattice rotation induced by a single dislocation is described by the following equation:

$$\Delta\theta_{single} = \mathrm{b/t} \tag{4}$$

The effective thickness in nanomaterials is limited by the specimen size. As illustrated experimentally by Hofmann *et al*. [27], a single dislocation line within a nanostructure induces a sharp change of the lattice rotation similar to a tilt boundary in a bulk specimen (see Fig. 6(a) and (b)). When two edge dislocations of two different slip systems are present in a nano-object (illustrated by the red and blue lines in Fig. 6(c)), each of them induces a separate rotation around its corresponding <112> axes. With different line directions, the two dislocations divide the crystal into four parts exhibiting four different combinations of rotations. This distribution of lattice rotations spreads the diffraction peak into two directions on the detector.

This manuscript was accepted by J. Appl. Phys. Click here to see the version of record.

For the $[01\bar{1}](111)$ and the $[101](\bar{1}11)$ slip systems observed in the nanowire, multiple dislocations are stored within the nanowire. As indicated by the blue and red lines in Fig. 6(d), the dislocation line for edge dislocations of $[01\bar{1}](111)$ type is perpendicular to the nanowire axis while it is tilted by 30° for the $[101](\bar{1}11)$ type dislocation. Considering a nanowire thickness of 90 nm, each $[01\bar{1}](111)$ and $[101](\bar{1}11)$ type dislocation induces a rotation of 0.18° around Au $[\bar{2}11]$ and 0.06° around Au $[12\bar{1}]$, respectively. Within the probed volume, for one rotation angle around the Au $[\bar{2}11]$ axis, a multitude of rotation angles around $[12\bar{1}]$ is present leading to the vertical lines separating the diffraction peaks in Fig. 5. The ratio of these two rotations differs across the nanowire width corresponding to the upper and lower border of the diffraction peak.

Connecting the positions with the same rotation angles on the two sides of the nanowire width (see Fig. S6(e) in the supplementary material), the distribution of the stored GNDs is extracted as presented by Fig. 6(e). A maximum of 15 $[01\bar{1}](111)$ and 6 $[101](\bar{1}11)$ type GNDs is found close to the left clamping point (position i) and the number of stored dislocations steadily decreases towards position ii. The angle between the line directions of the two slip systems varies between 27° and 58°. Considering only edge dislocation, the line direction is given by the slip system and the angle are thus fixed. In the case of dislocations with screw components, however, the line direction of the slip system is no longer fixed, which may generate the variation of the line directions. Taking this into account would, however, require three-dimensional calculations which are out of the scope of this work.

This manuscript was accepted by J. Appl. Phys. Click here to see the version of record.

5. Discussion

The traditional indexation process measures the crystalline orientation on a 3D real space grid allowing for decomposing the curvature tensor into contributions from different slip systems [9]. The peak shape analysis developed in this work can be considered as a projected 3D measurement of the crystalline orientation. Since there are only 9 independent components in Nye's tensor but 18 distinct dislocation types (edge and screw), no unique solution exists for the slip systems. However, considering the finite dimension of our specimen and the continuity of the dislocation lines within the specimen, the activation of the slip systems described above is the most reasonable solution.

Contrary to the findings by Laue micro-diffraction, the resolved shear stress (RSS) distribution, calculated for the 12 slip systems using FEM in the framework of continuum anisotropic elasticity considering the complete experimental configuration (angle between nanowire and Si micro-trench, misalignment of SFINX tip) for Δz = 1100 nm is maximal for the $[\bar{1}01](1\bar{1}1)$, $[110](1\bar{1}1)$, $[101](\bar{1}\bar{1}1)$, and $[\bar{1}10](\bar{1}\bar{1}1)$ slip systems (see Fig. 7). It is thus similar to a perfect plane strain bending (see Table 1 in the supplementary material) despite a significant amount of torsion being present during the *in-situ* three-point bending test and tilt of the nanowire with respect to the Si support. Therefore, in spite of a very precise account of the imperfections of the nanomechanical test, they cannot account for the observed plastic behavior. The discrepancy of our experimental findings with respect to the simulations might be related to the dislocation nucleation process within the nanowire. Actual three-point bending tests contain points of stress concentrations at the loading position and at the clamping points (as illustrated by maximal RSS at these positions in Fig. 7).

This manuscript was accepted by J. Appl. Phys. Click here to see the version of record.

At the loading position (between position ii and iii in the *post-mortem* diffraction map), a kink is observed after plastic deformation. While the *post-mortem* SEM image may suggest a glide band where most of the dislocations escaped at the nanowire free surfaces, the non-detectable low diffraction intensity at this position indicates a strongly perturbed crystalline lattice caused by the storage of a large number of stored GNDs at this position. Comparing the integrated Laue micro-diffraction patterns recorded *in-situ* with the *post-mortem* pattern provides further information on the starting point and the evolution of plasticity. A sequence of the integrated Au 331 diffraction peak extracted from the left-hand side of the loading point for piezo movements of 1100, 1200, and 1300 nm are presented in Fig. 8(a), (b), and (c), respectively. With increasing load, the shape as well as the movement of the diffraction peak gradually approaches the one after unloading, which is indicated by yellow lines (position i to ii in the *post-mortem* diffraction map). As pointed out by Kirchlechner *et al* [18], in the nanomaterial this broadening may be caused either by the storage of dislocations or by an inhomogeneous strain distribution. While the broadening of the diffraction peak for $\Delta z \geq 1200$ nm is mainly due to the storage of GNDs, the slight deviation of the peak shape and the increased peak width at highest load ($\Delta z = 1300$ nm) are attributed to a remaining torsion and an additional inhomogeneous strain within the loaded nanowire, respectively. The less pronounced streaking of the diffraction peaks from the Si support towards position ii implies that the GND density diminishes (see also Fig. 5(a)). Hence, it is reasonable to assume that dislocations observed after unloading are nucleated at the clamping position. As demonstrated in section 4, the streaking of the Laue spots mainly corresponds to the rotation of the Au crystalline lattice. In the vicinity of the clamping point, the peak broadening remains the same during and after

This manuscript was accepted by J. Appl. Phys. Click here to see the version of record.

lacing indicating that the local lattice rotation at this position does not change. Thus, at this position the GNDs are stored according to the curvature tensor as described by Nye [9]. Along the nanowire, the broadening gradually spreads from the clamping point. The final GND distribution might thus not only be influenced by the stress state determined by the complete wire profile, but also by the local rotation at the nucleation position. The local rotation in the vicinity of the clamping point is affected by the orientation the nanowire with respect to the Si ridges which is about 114˚ as illustrated in Fig. 1. Since the Si ridges are more rigid than the Au nanowire, their edges impose a certain shape to the bent nanowire which differs from a perfect three-point bending test, thus leading to localized rotations. As shown by the FEM simulations in Fig. 3(b), slight variations of the torsion exist close to the two clamping points, which deviate from the linear increase observed in the rest of the nanowire. The unexpected slip systems are energetically the most favorable ones accommodating the best the deformation geometry in the vicinity of the clamping. They might be the L^2 minimized solutions for Nye's tensor at the clamping point [9].

Before the discontinuity in the evolution of the integrated diffraction patterns at Δz = 1200 nm (Fig. 8(a)), broadened diffraction peaks are already observed near the Si support, which might be related to the nucleation of dislocations. While the *in-situ* study presented here shows the overall behavior (elastic and plastic) of the Au nanowire during a three-point bending test, the loading steps are too coarse to detect the very first dislocations nucleated and stored within the nanowire. In addition, the inhomogeneous elastic strain within the bent nanowire broadens the diffraction peaks and, thus hinders the detection of the first defects. Therefore, dedicated

in-situ investigations are needed with smaller loading steps and intermittent unloading to verify the elastic deformation and determine the nature of the GNDs at the clamping points.

6. Conclusions

In conclusion, the elastic and plastic properties of three-point bent Au nanowires are investigated by *in-situ* Laue micro-diffraction. A new data treatment method employing the integration of Laue micro-diffraction patterns is described, which allows for visualizing the movement of the diffraction peaks along the nanowire and extract the actual elastic and plastic deformation. For the elastic deformation, both bending and torsion are present. While the former is evidently expected, the latter is caused by a misalignment of the SFINX-tip with respect to the center of the nanowire width of the order of 60 nm. For the plastic deformation, detailed peak shape analysis further allows for counting the number of stored dislocations and points to the activation of the $[01\bar{1}](111)$ and the $[101](\bar{1}11)$ slip system which are unexpected and in contradiction with recent MD simulations predicting the formation of wedge-shaped twins [11] as well as with the calculated critical resolved shear stresses. The experimental findings suggest that for defect-scarce nanomaterials, the final GNDs distributions might be influenced not only by the complete deformation profile, but also by the local rotation field at the dislocation nucleation position. Further insight in the plasticity of three-point bent nanostructures may be obtained by future dedicated experiments concentrating on the nucleation of the very first dislocations as well as by three-dimensional atomistic simulations.

Supplementary Material

The supplementary online material demonstrates the background subtraction of Laue micro-diffraction patterns, thus removing the Si Laue spots from the substrate and enhancing the visibility of the Laue diffraction peaks originating from the Au nanowire. It further describes the calculation of one-dimensional orientation maps from Laue diffraction patterns and gives additional details on the finite element method simulations. The analysis of the shape of the diffraction peaks that is introduced in this paper is further described and additional information on the determination of the activated slip systems is given. Moreover, a table with the Schmid factors for the tensile side of a bent nanowire is presented.

Acknowledgements

The authors gratefully acknowledge the financial support from the French National Research Agency through the project ANR-11-BS10-01401 MecaniX. They further thank the French CRG program committee for the allocated beamtime at the BM32 beamline at ESRF.

References

[1] S.S. Brenner, J. Appl. Phys. 27, 1484–1491 (1956).

[2] C. Herring, J.K. Galt, Phys. Rev. 85, 1060–1061 (1952).

[3] G. Richter, K. Hillerich, D.S. Gianola, R. Mönig, O. Kraft, C.A. Volkert, Nano Lett. 9, 3048–3052(2009).

[4] H. Bei, S. Shim, E.P. George, M.K. Miller, E.G. Herbert, G.M. Pharr, Scr. Mater. 57, 397–

400 (2007).

[5] S.H. Oh, M. Legros, D. Kiener, G. Dehm, Nat. Mater. 8, 95 (2009).

[6] S. Lee, J. Im, Y. Yoo, E. Bitzek, D. Kiener, G. Richter, B. Kim, S.H. Oh, Nat. Commun. 5, 3033 (2014).

[7] B. Roos, B. Kapelle, G. Richter, C.A. Volkert, Appl. Phys. Lett. 105, 201908 (2014).

[8] A. Sedlmayr, E. Bitzek, D.S. Gianola, G. Richter, R. Mönig, O. Kraft, Acta Mater. 60, 3985–3993 (2012).

[9] J.F. Nye, Acta Metall. 1, 153–162 (1953).

[10] P.J. Konijnenberg, S. Zaefferer, D. Raabe, Acta Mater. 99, 402–414(2015).

[11] W.G. Nöhring, J.J. Möller, Z. Xie, E. Bitzek, Extrem. Mech. Lett. 8, 140–150(2016).

[12] Y.G. Zheng, H.W. Zhang, Z. Chen, L. Wang, Z.Q. Zhang, J.B. Wang, Appl. Phys. Lett. 92, 41913(2008).

[13] E. Demir, F. Roters, D. Raabe, J. Mech. Phys. Solids. 58, 1599–1612(2010).

[14] E. Demir, D. Raabe, F. Roters, Acta Mater. 58, 1876–1886(2010).

[15] J. Gong, T. Benjamin Britton, M.A. Cuddihy, F.P.E. Dunne, A.J. Wilkinson, Acta Mater. 96, 249–257(2015).

[16] C. Motz, T. Schöberl, R. Pippan, Acta Mater. 53, 4269–4279(2005).

[17] D. Kiener, C. Motz, W. Grosinger, D. Weygand, R. Pippan, Scr. Mater. 63, 500–503 (2010).

[18] C. Kirchlechner, W. Grosinger, M.W. Kapp, P.J. Imrich, J.-S. Micha, O. Ulrich, J. Keckes, G. Dehm, C. Motz, Philos. Mag. 92, 3231–3242(2012).

[19] Z. Ren, F. Mastropietro, A. Davydok, S. Langlais, M.-I. Richard, J.-J. Furter, O. Thomas, M. Dupraz, M. Verdier, G. Beutier, P. Boesecke, T.W. Cornelius, J. Synchrotron Radiat. 21,

1128–1133 (2014).

[20] C. Leclere, T.W. Cornelius, Z. Ren, A. Davydok, J.-S. Micha, O. Robach, G. Richter, L. Belliard, O. Thomas, J. Appl. Crystallogr. 48, 291–296 (2015).

[21] C. Leclere, T.W. Cornelius, Z. Ren, O. Robach, J.-S. Micha, A. Davydok, O. Ulrich, G. Richter, O. Thomas, J. Synchrotron Radiat. 23, 1395–1400 (2016).

[22] J.-S. Micha, LaueTools: Open Source Python Packages for X-ray MicroLaue Diffraction Analysis., (2014).

[23] T.J. Hardin, B.L. Adams, D.T. Fullwood, R.H. Wagoner, E.R. Homer, Int. J. Plast. 50, 146–157 (2013).

[24] J.W. Huang, J.C. E, J.Y. Huang, T. Sun, K. Fezzaa, S.N. Luo, J. Synchrotron Radiat. 23, 712–717 (2016).

[25] R.I. Barabash, G.E. Ice, F.J. Walker, J. Appl. Phys. 93, 1457–1464 (2003).

[26] R. Barabash, G.E. Ice, B.C. Larson, G.M. Pharr, K.-S. Chung, W. Yang, Appl. Phys. Lett. 79, 749–751(2001).

[27] F. Hofmann, B. Abbey, W. Liu, R. Xu, B.F. Usher, E. Balaur, Y. Liu, Nat. Commun. 4, 2774 (2013).

[28] J. Petit, O. Castelnau, M. Bornert, F.G. Zhang, F. Hofmann, A.M. Korsunsky, D. Faurie, C. Le Bourlot, J.S. Micha, O. Robach, O. Ulrich, J. Synchrotron Radiat. 22, 980–994 (2015).

[29] B.C. Larson, W. Yang, G.E. Ice, J.D. Budai, J.Z. Tischler, Nature. 415, 887(2002).

Figure Captions

Fig. 1: (a) Schematic diagram of experimental configuration at BM32. (b) Scanning electron microscopy image of a self-suspended Au nanowire before deformation. The measurement positions along the nanowire during KB scans are marked by rectangles and the scanning direction is indicated by the arrow.

Fig. 2: Integrated background-subtracted Laue micro-diffraction patterns of KB scans recorded at the piezo movement of (a) 0 nm, (b) 400 nm, (c) 800 nm, (d) 1100 nm, (e) 1200 nm, and (f) 1300 nm. The insets show an enlarged view of the areas around the Au 222 Laue spot. The red full dots in (d) represent the positions of the Laue diffraction spots for a bent and twisted nanowire as presented in Fig. 3(b).

Fig. 3: (a) Enlarged view of the area around the Au 222 diffraction peak at the piezo movement of 1100 nm. The expected movements of the Laue spot on the detector for a pure vertical bending (rotation around Au $[211]$ direction) and a pure torsion (rotation around Au $[01\bar{1}]$ direction) are marked as red and black lines, respectively. (b) Bending and torsion profile along the suspended part of the nanowire inferred from the integrated Laue micro-diffraction pattern shown in (a) and calculated by finite element method simulations taking into account a force of 2.1 μN and a misalignment of the SFINX-tip with respect to the nanowire center of 57 nm. The peak-to-peak value of (c) the bending and (d) torsion angles estimated from the path of the Au 222 Laue spot plotted with respect to the ones obtained from the FEM simulation.

Fig. 4: (a) 1D orientation map of the plastically deformed Au nanowire superimposed on the *post-mortem* SEM image. (b) Corresponding integrated background-subtracted Laue micro-diffraction pattern recorded along the suspended nanowire (from position i to iv in Fig. 4(a)).

Fig. 5: Integrated diffraction patterns from position i to ii in Fig. 4 of (a) the Au 222, and (b) the Au 442 Laue spot. Integrated diffraction patterns from position iii to iv of (c) the Au 222, (d) the Au 442 Laue spot. The yellow lines mark the expected peak shapes generated by linearly combining rotations around the Au $[\bar{2}11]$ and the Au $[12\bar{1}]$ axes.

Fig. 6: Schematic illustration of the lattice rotation induced by a single edge dislocation: (a) side view, (b) top view. (c) The rotation combination due to two single edge dislocations of different slip system. (d) Schematic illustration of the rotation field caused by the two type of dislocations (top view). The probed volume illuminated by the X-ray beam is marked by the pink rectangular. Blue and red lines correspond to the stored $[01\bar{1}](111)$ type and $[101](\bar{1}11)$ type of dislocations. (e) The distribution of the GNDs from position i to ii along the nanowire extracted from the peak shape analysis.

Fig. 7: The resolved shear stress distribution along the nanowire for the 12 slip systems in the FCC crystal, calculated from 2nd Piola-Kirchoff stress tensor obtained in the FEM simulation. The top and back view corresponds to the top and bottom surface of the nanowire, where the highest stress is observed.

Fig. 8: The Au 331 diffraction peak integrated from the left Si support to the loading position recorded at the piezo movement of: (a) 1100 nm, (b) 1200 nm, and (c) 1300 nm. The red arrows indicate the movement direction of the diffraction peaks from the Si support to the loading point. The yellow lines mark the peak shape from position i to ii in the *post-mortem* diffraction map.

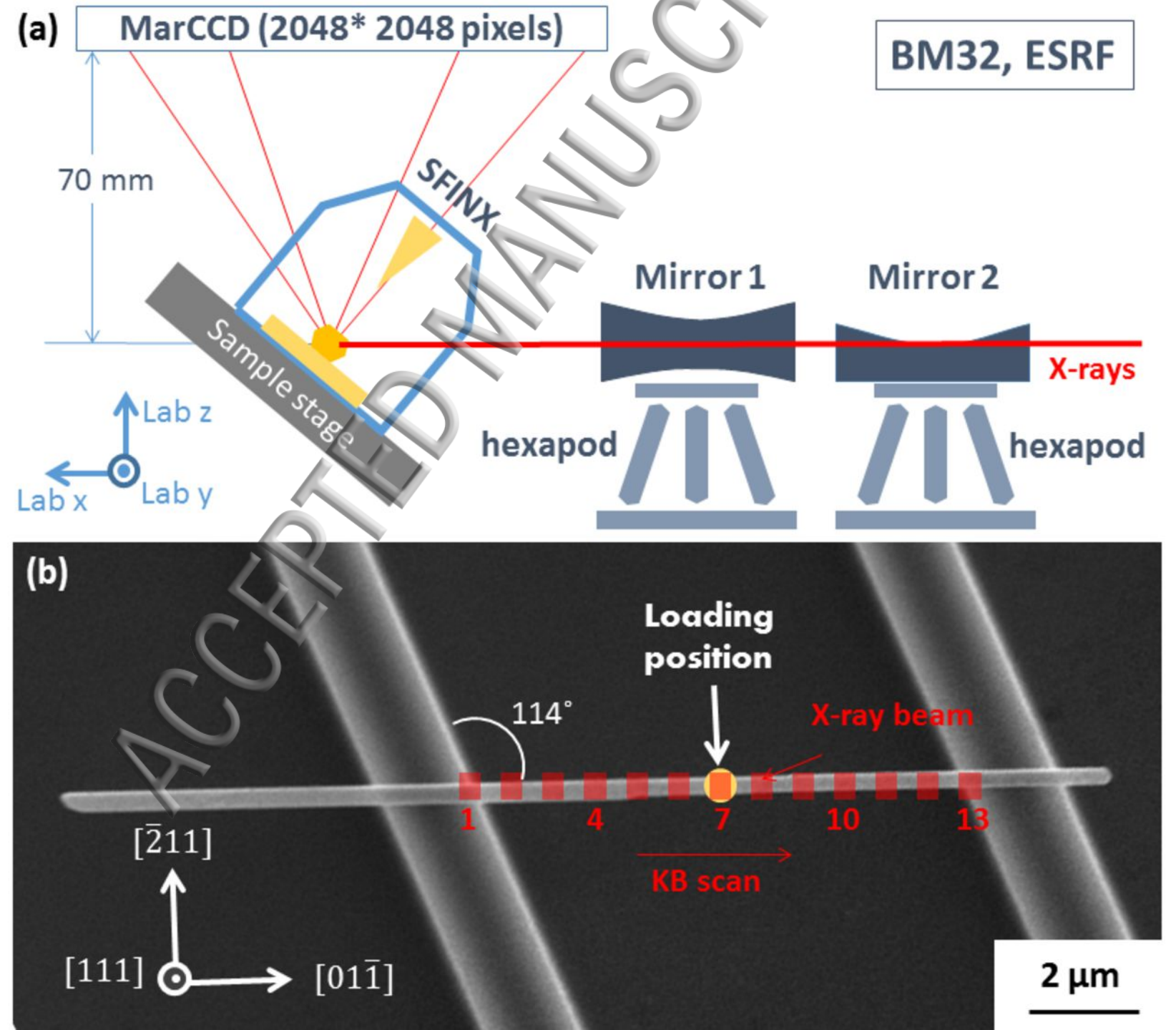

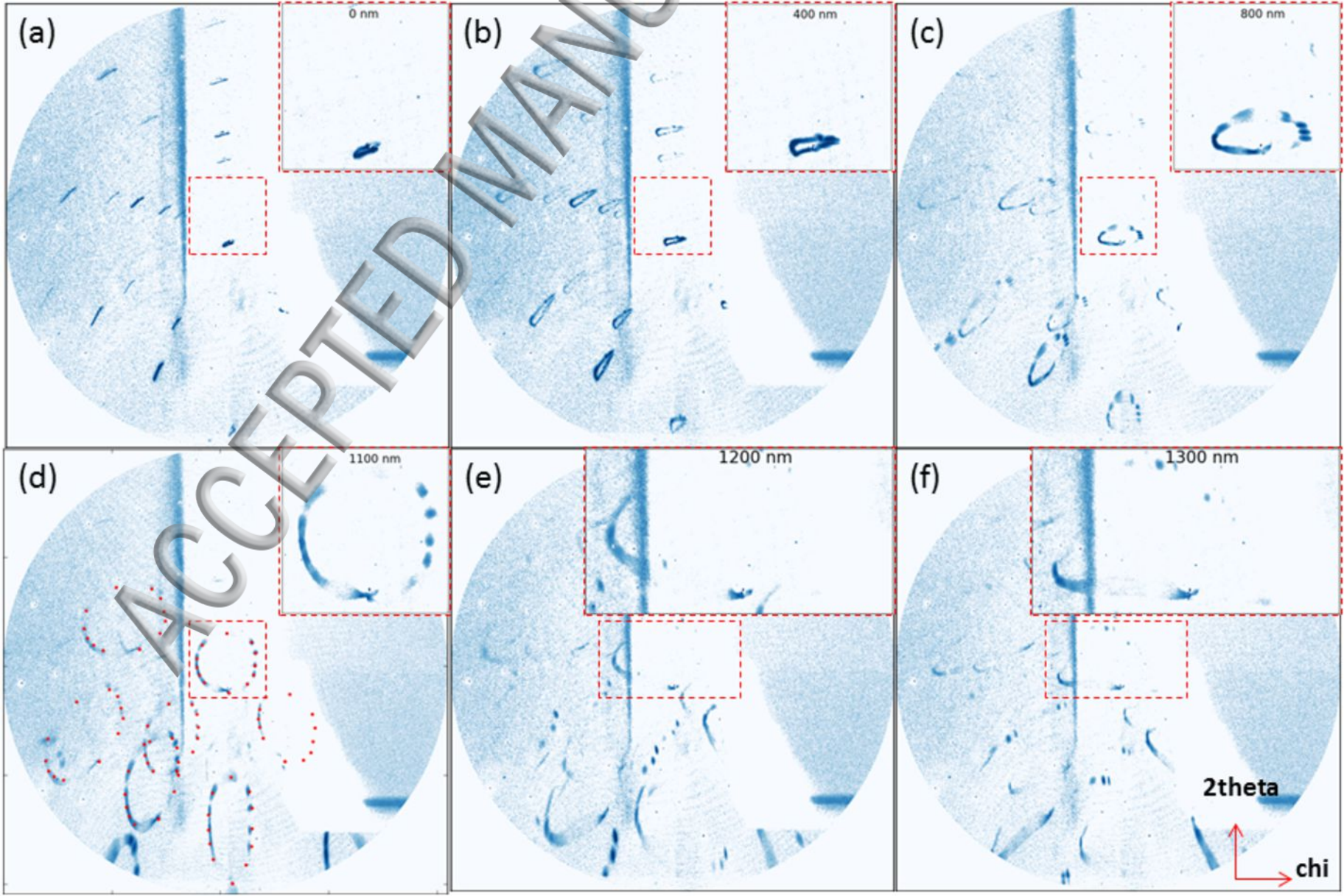

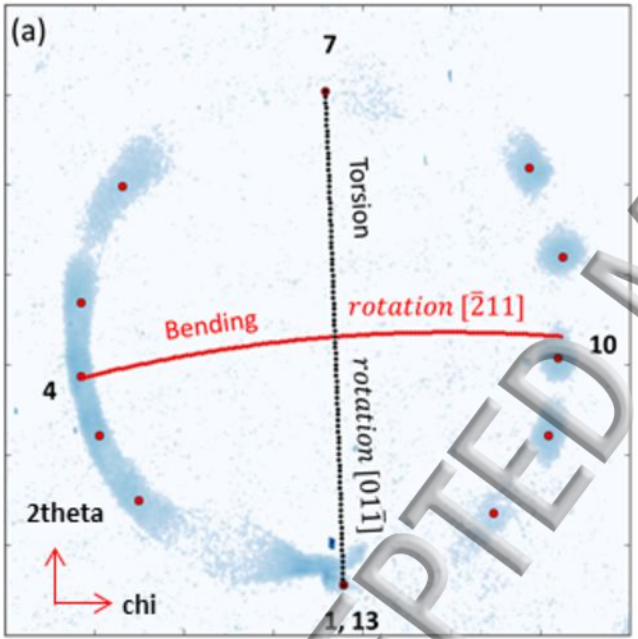

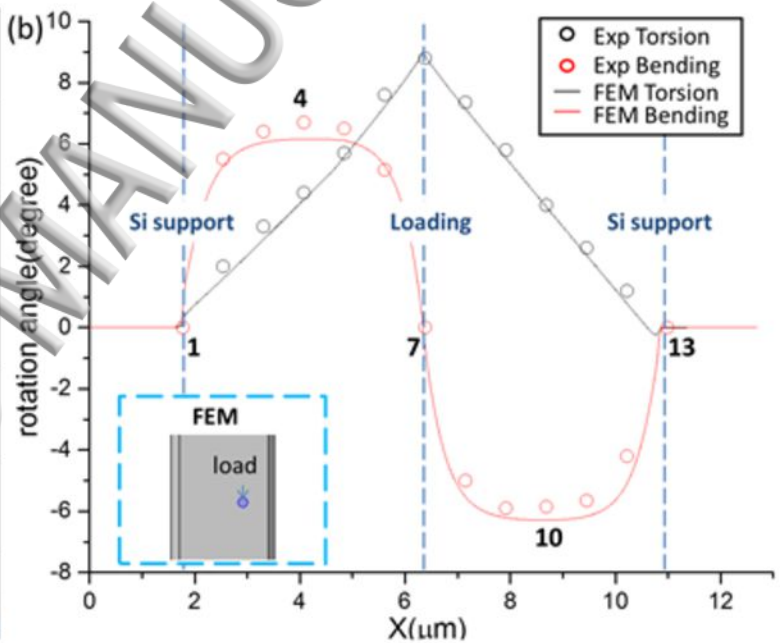

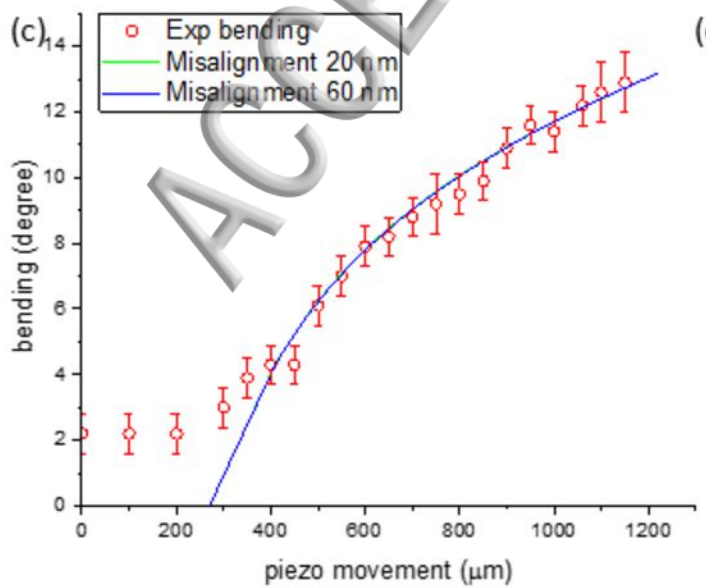

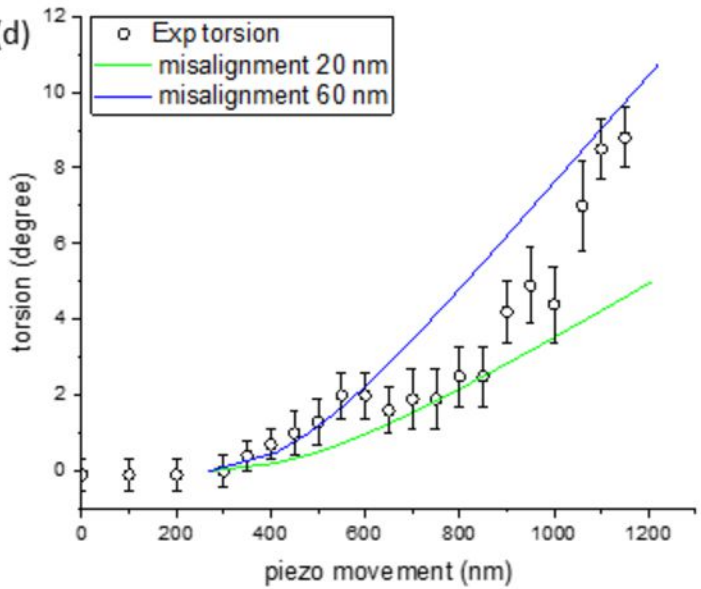

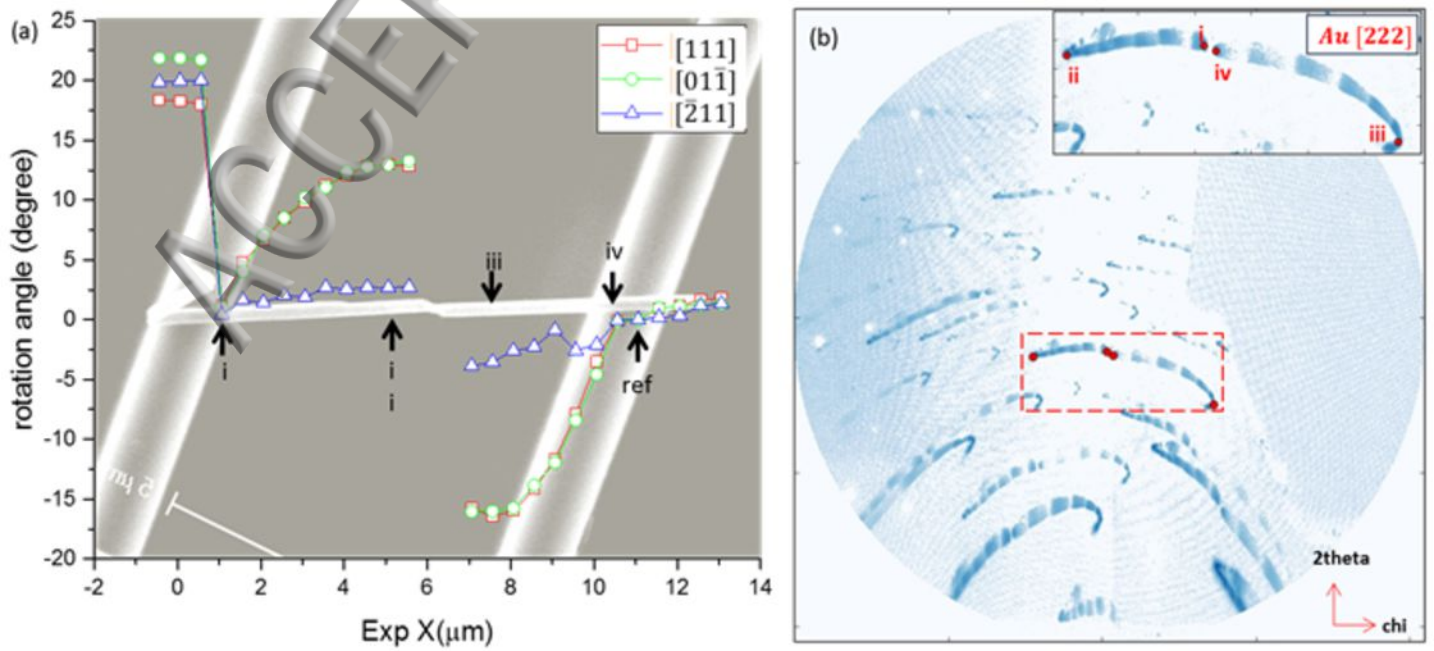
(a)
rotation angle (degree)
Exp X(μm)
[111]
[01$\bar{1}$]
[$\bar{2}$11]
i
i
i
iii
iv
ref
(b)
Au [222]
i
ii
iii
iv
2theta
chi

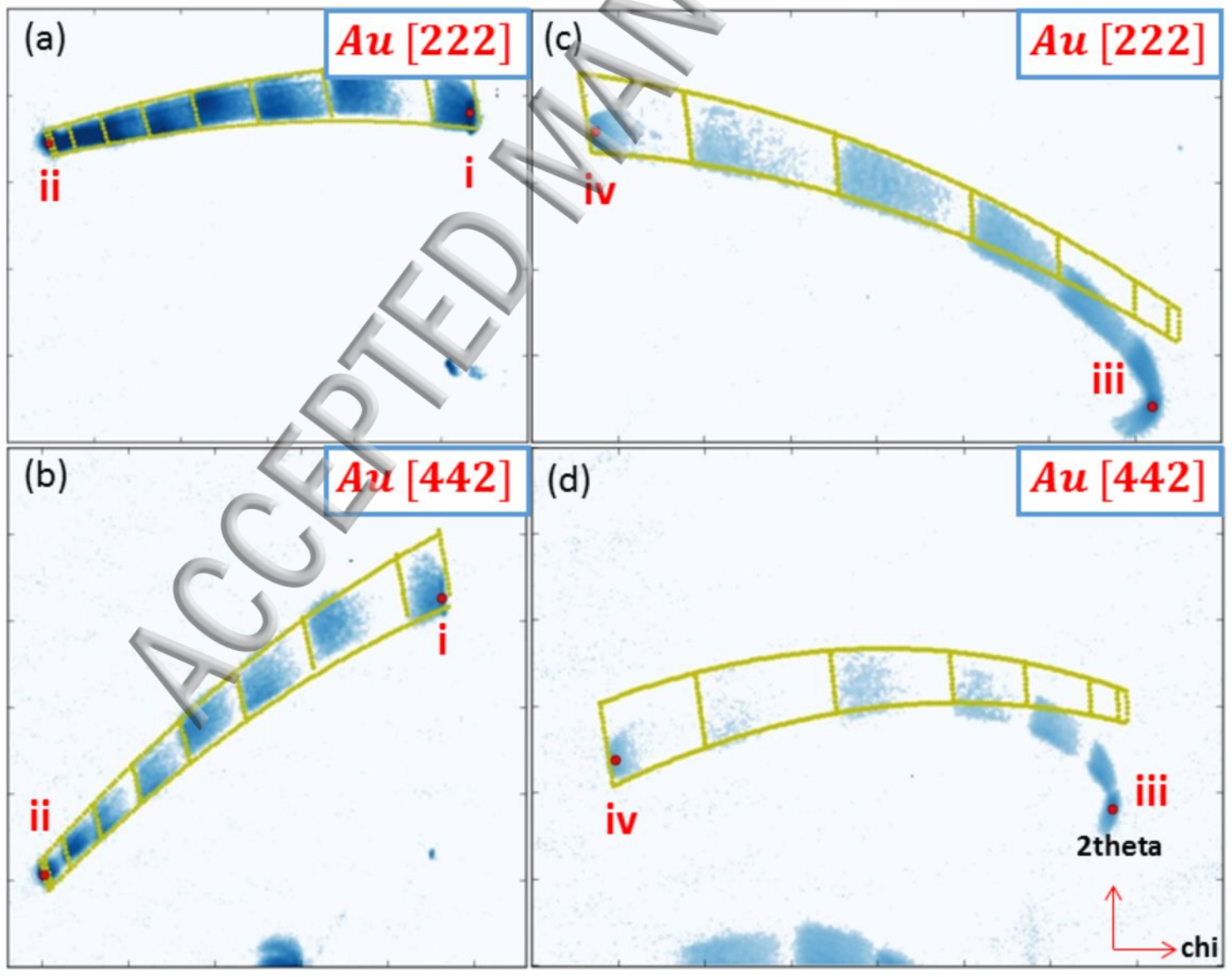

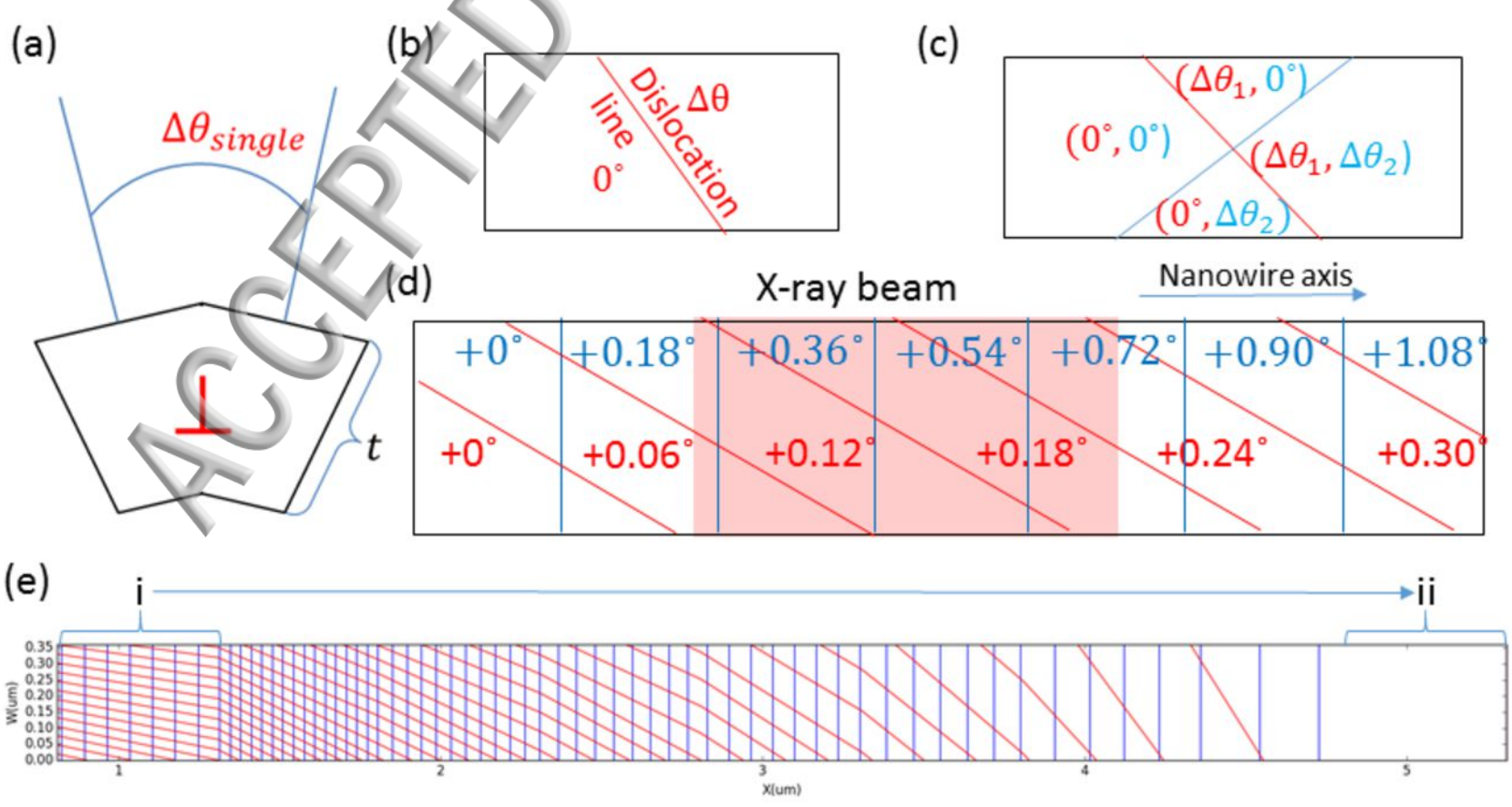
(a)
$\Delta\theta_{single}$
t
(b)
Dislocation line
Δθ
0°
(c)
$(\Delta\theta_1, 0^\circ)$
$(0^\circ, 0^\circ)$
$(\Delta\theta_1, \Delta\theta_2)$
$(0^\circ, \Delta\theta_2)$
(d)
X-ray beam
Nanowire axis
+0°
+0.18°
+0.36°
+0.54°
+0.72°
+0.90°
+1.08°
+0°
+0.06°
+0.12°
+0.18°
+0.24°
+0.30°
(e)
i
ii
W(um)
X(um)

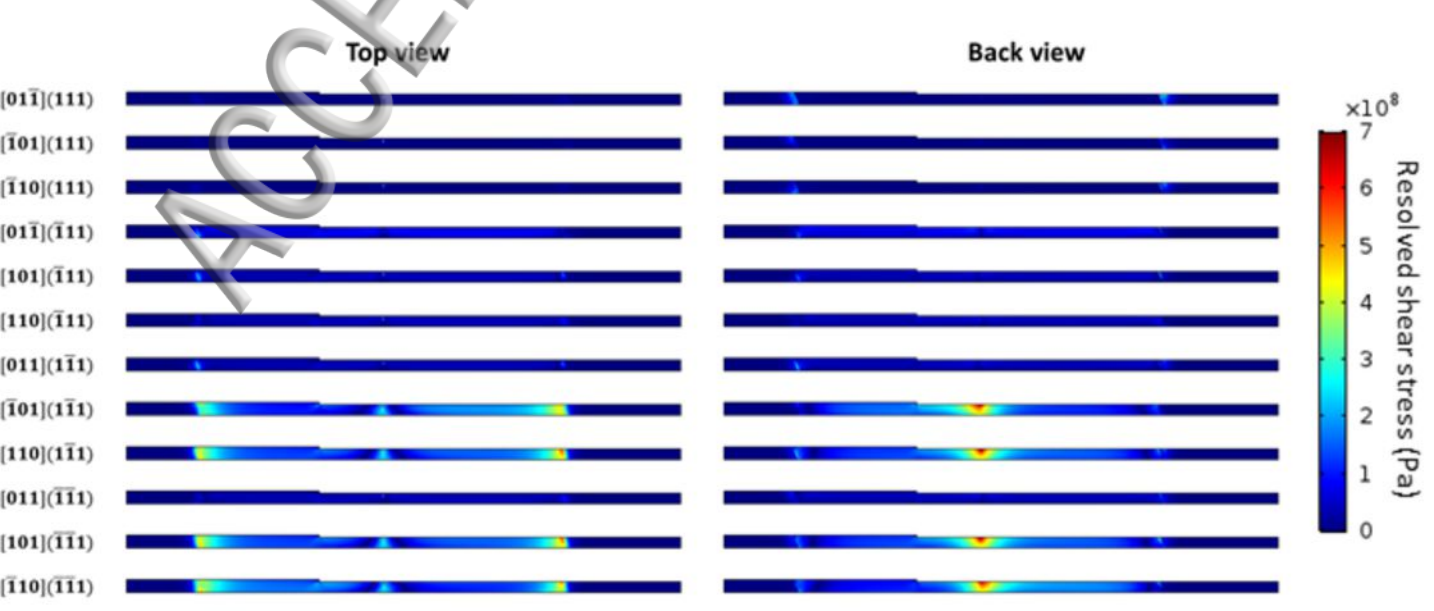
Top view
Back view
[01$\bar{1}$](111)
[$\bar{1}$01](111)
[$\bar{1}$10](111)
[01$\bar{1}$]($\bar{1}$11)
[101]($\bar{1}$11)
[110]($\bar{1}$11)
[011](1$\bar{1}$1)
[$\bar{1}$01](1$\bar{1}$1)
[110](1$\bar{1}$1)
[011]($\bar{1}\bar{1}$1)
[101]($\bar{1}\bar{1}$1)
[$\bar{1}$10]($\bar{1}\bar{1}$1)
×10^8
7
6
5
4
3
2
1
0
Resolved shear stress (Pa)

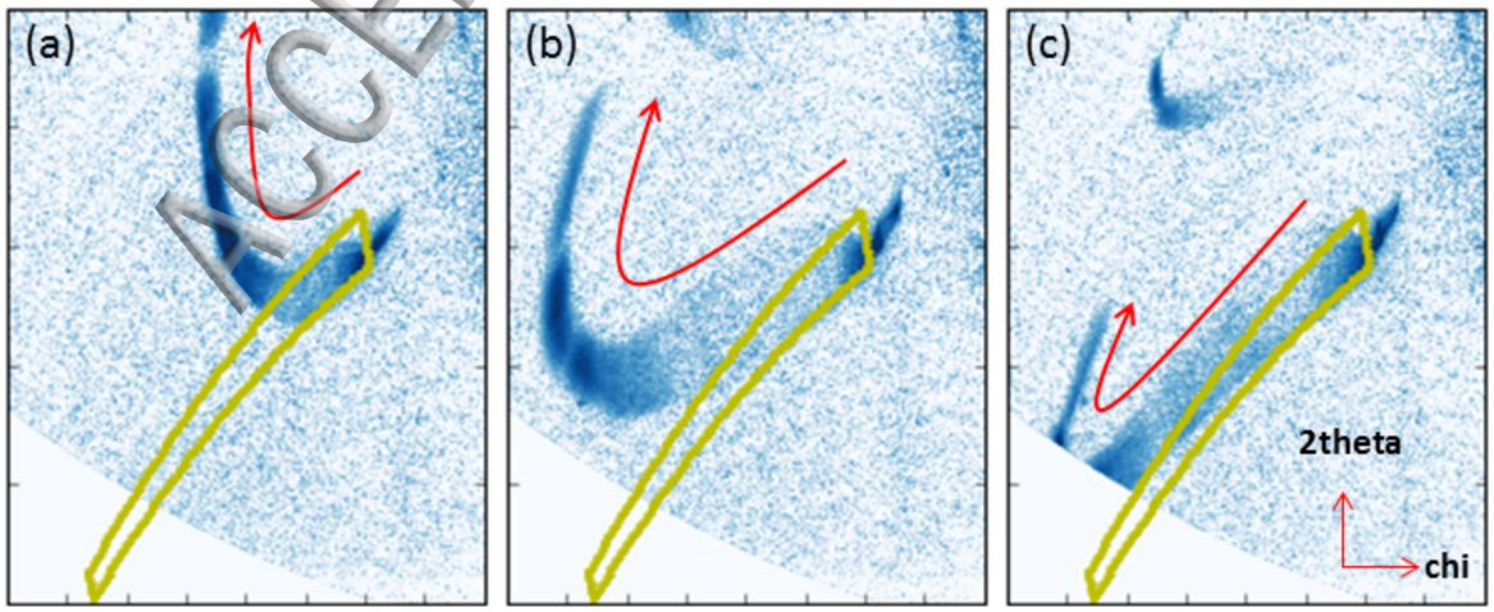
(a)
(b)
(c)
2theta
chi